



Article

Reducing the Residual Topography Phase for the Robust Landscape Deformation Monitoring of Architectural Heritage Sites in Mountain Areas: The Pseudo-Combination SBAS Method

Hang Xu ¹, Fulong Chen ^{2,3,*}, Wei Zhou ^{2,3} and Cheng Wang ³¹ School of Earth and Space Sciences, Peking University, Beijing 100871, China; hangx@stu.pku.edu.cn² International Research Center of Big Data for Sustainable Development Goals, Beijing 100094, China; zhouwei@aircas.ac.cn³ Key Laboratory of Digital Earth Science, Aerospace Information Research Institute, Chinese Academy of Sciences, Beijing 100094, China; wangcheng191@mails.ucas.ac.cn

* Correspondence: chenfl@aircas.ac.cn

Abstract: Monitoring deformation of architectural heritage sites is important for the quantitative evaluation of their stability. However, deformation monitoring of sites in mountainous areas remains challenging whether utilizing global navigation satellite system (GNSS) or interferometric synthetic aperture radar (InSAR) techniques. In this study, we improved the small baseline subset (SBAS) approach by introducing the pseudo-baseline combination strategy to avoid the errors caused by inaccurate external DEM, resulting in robust deformation estimations in mountainous areas where the architectural heritage site of the Great Wall is located. First, a simulated dataset and a real dataset were used to verify the reliability and effectiveness of the algorithm, respectively. Subsequently, the algorithm was applied in the landscape deformation monitoring of the Shanhaiguan section of the Great Wall using 51 Sentinel-1 scenes acquired from 2016 to 2018. A thematic stability map of the Shanhaiguan Great Wall corridor was generated, revealing that the landscape was generally stable save for local instabilities due to unstable rocks and wall monuments. This study demonstrated the capabilities of adaptive multitemporal InSAR (MTInSAR) approaches in the preventive landscape deformation monitoring of large-scale architectural heritage sites in complex terrain.

Keywords: InSAR; architectural heritage; pseudo-combination; residual topography



Citation: Xu, H.; Chen, F.; Zhou, W.; Wang, C. Reducing the Residual Topography Phase for the Robust Landscape Deformation Monitoring of Architectural Heritage Sites in Mountain Areas: The Pseudo-Combination SBAS Method. *Remote Sens.* **2022**, *14*, 1178. <https://doi.org/10.3390/rs14051178>

Academic Editor: Bruce D. Chapman

Received: 20 January 2022

Accepted: 25 February 2022

Published: 27 February 2022

Publisher's Note: MDPI stays neutral with regard to jurisdictional claims in published maps and institutional affiliations.



Copyright: © 2022 by the authors. Licensee MDPI, Basel, Switzerland. This article is an open access article distributed under the terms and conditions of the Creative Commons Attribution (CC BY) license (<https://creativecommons.org/licenses/by/4.0/>).

1. Introduction

Using satellites as platforms, spaceborne remote sensing technologies can gather large-scale ground information without contacting the targets, which is both cost-effective and labor-saving [1,2]. As one branch of active spaceborne remote sensing, spaceborne synthetic aperture radar (SAR) uses microwaves to acquire ground surface information and can work night and day and in all weather conditions [3,4]. Based on the phase information of SAR signals, interferometry synthetic aperture radar (InSAR) has the ability to monitor ground deformation with millimeter accuracy [5]. To date, InSAR has been widely used in land surface deformation monitoring, including landslide monitoring, urban surface settlement monitoring, and infrastructure (e.g., railways and bridges) deformation monitoring [6–10].

Our architectural heritage is an important cultural and spiritual symbol of our ancestors and has immeasurable value. However, due to the combined impacts of natural erosion and anthropogenic activities, a substantial number of cultural heritage structures exhibit health problems [11–14]. Therefore, reliable deformation monitoring of heritage structures and their surroundings is important for health assessments and stability monitoring of these historical properties [15–18]. Traditional geodetic measurements such as those from global navigation satellite systems (GNSS) and leveling, and other on-site

observations [19,20] can detect subtle changes in position, but they have certain limitations (i.e., sparse measurements in space and time- and labor-intensive) and are mainly used for deformation detection at a single-monument scale. Thus, a geodetic technology capable of monitoring deformation of an extended area while providing density measurements can be a powerful tool for the conservation of heritage sites over larger areas [21].

In the past decade, studies have demonstrated the power of InSAR as a tool for the deformation monitoring of cultural heritage structures, which can complement traditional geodetic measurements [21–25]. Since the topography phase and deformation phase are mixed in the InSAR signal [26], it is necessary to introduce external digital elevation models (DEM) in the differential operation of InSAR to mitigate the topography-related phase [27]. However, the error of external DEM can introduce the residual topographic phase in the differential interferograms, especially in mountainous areas [28–30]. This interferes with the acquisition of fine-scale deformation measurements of large-scale heritage sites, especially in mountainous areas (e.g., the Great Wall).

To solve the aforementioned problem, the residual topography phase is normally modeled as a parameter and estimated simultaneously alongside the deformation phase in MTInSAR [31,32]. However, this approach relies on there being a suitable distribution of baselines, and its performance is limited [28]. Samsonov provided two different methods for the estimation of the InSAR DEM error [33], which is useful when the perpendicular baselines of SAR data are large and variable (e.g., L-band ALOS PALSAR data); Fattahi and Amelung [34] estimated the residual topography in the InSAR time domain, but this method relies on an empirical temporal deformation. Furthermore, in some InSAR applications in smaller areas, high-precision DEM had to be generated in advance to mitigate the topography effect caused by inaccurate external DEM [26], but generating high-resolution DEM data is costly and increases the complexity of data processing. Recently, Zhang et al. proposed the pseudo-baseline combination algorithm, wherein interferograms were combined twice based on the perpendicular baseline before being used for deformation estimation with the temporarily coherent points (TCP) technology [35]. This approach effectively mitigated the unexpected heights phase caused by skyscrapers in urban areas, but the density of candidate points is limited in applications in mountainous areas.

In this study, we proposed an improved small baseline subset (SBAS) algorithm based on a pseudo-baseline combination strategy to reduce the residual topography effect in mountainous areas caused by inaccurate external DEM. Separate tests using simulated and measured datasets were used to verify the reliability and effectiveness of the approach. After verification, this approach was applied to the Shanhaiguan Great Wall and its surroundings in China, producing a robust landscape deformation estimation in a mountainous region.

2. Methods

The workflow of the pseudo-combination SBAS method is illustrated in Figure 1. First, pairs of input SAR images with small spatio-temporal baseline thresholds were selected to ensure the coherence of the interferograms. Then, the SAR pairs were preprocessed, including coregistration, interferometry, multilooking, and filtering. Subsequently, the unwrapped interferograms were combined twice based on their perpendicular baselines to generate pseudo-baseline interferograms with vertical baselines close to 0; thus, the residual topography phase was suppressed. Finally, the deformations in time series were solved based on the pseudo-baseline interferograms. Note that the interferograms were unwrapped before the pseudo-baseline combination; thus, the pseudo-combination SBAS method does not introduce extra error in unwrapping step. The details of this method are introduced in the following sections.

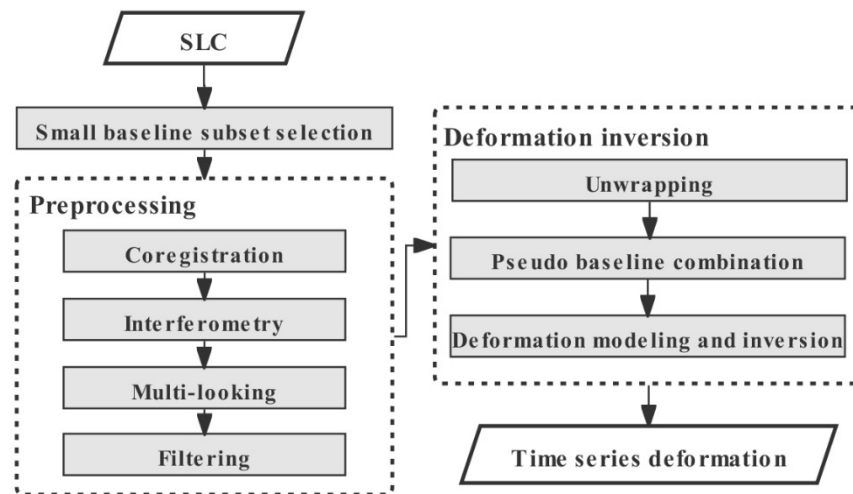


Figure 1. Work flow of the pseudo-combination SBAS method.

Assuming $N + 1$ SAR images covering the same area are obtained, their spatio-temporal baselines are estimated, and the images are coregistered before the SAR pairs can be selected according to the spatio-temporal baseline thresholds. The number of interferograms (M) can be expressed by the following inequality [32]:

$$\frac{N + 1}{2} \leq M \leq N \left(\frac{N + 1}{2} \right) \quad (1)$$

After the generation of differential interferograms, multilooking [36] and filtering are applied to the interferograms to reduce noise and improve image coherence. Subsequently, the interferograms are unwrapped to retrieve the relative phase of adjacent points from the wrapped phase. The relationship between the theoretical deformation phase (ϕ) and the differential interference phase of SAR images ($\delta\phi$) can be established as follows:

$$A\phi = \delta\phi$$

$$A = \begin{bmatrix} 1 & 0 & 0 & -1 & \dots \\ 0 & 1 & -1 & 0 & \dots \\ \dots & \dots & \dots & \dots & \dots \\ \dots & \dots & \dots & \dots & \dots \end{bmatrix} \quad (2)$$

where A is an $M \times N$ coefficient matrix that shows the combined integers of the original SAR data.

Normally, the deformation field could then be estimated either by the least squares method or singular-value decomposition method [32]. However, due to the limitations of DEM accuracy and coregistration accuracy, residual topography error may exist in the differential phase of interferograms when implementing two-pass differential interferometry [37]. Taking the widely used SRTM data as an example, the elevation error at 90% of the sampling points was within 7.4 m, and this error will increase in mountainous areas [38], which can introduce a residual topographic phase into the interferograms.

The relationship between residual topography (ϵ) and its phase in interferograms (ϕ_{topo_err}) can be expressed as follows:

$$\phi_{topo_err} = -\frac{4\pi}{\lambda} \frac{B_{\perp} \epsilon}{\rho \sin \theta} \quad (3)$$

where B_{\perp} denotes the perpendicular baseline; ρ denotes the slant range between satellite and ground objects; and θ is the incidence angle of the SAR signal. According to the formula, residual topography phase is mainly determined by the perpendicular baseline

and DEM error. Since the DEM error is certain, decreases in the perpendicular baseline can lead to decreases in the residual topography phase.

By combining the differential interferograms twice, the pseudo-baseline combination technology generates pseudo-baseline interferograms with vertical baselines close to 0; thus, the residual topography phase can be ignored during the following InSAR process. This strategy effectively mitigates the topography-related noise in the InSAR deformation field [35].

$$\phi_{pseudo} = a \cdot \phi_n + b \cdot \phi_m \quad (4)$$

where ϕ_{pseudo} is the phase of the pseudo-combined interferograms; ϕ_n and ϕ_m are the differential phases of the two input interferograms; and a and b are the corresponding integer combination coefficients. With the combined interferograms, the residual topography can be safely ignored in the following process. Unlike the approach proposed by Zhang et al. [35], the coefficients (i.e., a and b) are not limited to integers in our pseudo-combination SBAS method, and the perpendicular baseline of the pseudo-combined interferograms can approach 0 through the noninteger combination of interferograms. This is because phase unwrapping is completed before the interferograms are combined. However, in this study, the combination coefficients are still limited to integers to simplify the calculation.

The relationship between InSAR phase and deformation can be expressed using Equation (5) [35]:

$$\phi_{pseudo} = -\frac{4\pi}{\lambda} \left(a \sum_{m=IS_m}^{IP_m} t_m v_m + \sum_{p=IS_p}^{IP_p} t_p v_p \right) \quad (5)$$

where t_m and t_p are the time intervals of the two respective input interferograms; v_m and v_p are the corresponding surface deformation rates to be solved; IP_m and IS_m are the indexes of primary and secondary SAR images in m th interferogram, respectively; and IP_p and IS_p are the indexes of primary and secondary SAR images in p th interferogram, respectively. Assuming the number of input SAR images covering the same area is $N + 1$, the deformation velocity vector (V) can be expressed as follows:

$$V = [v_1, \dots, v_N] \quad (6)$$

Thus, the relationship between the pseudo-combined phase vector ϕ_{pseudo} and the deformation velocity vector V can be expressed as a linear equation:

$$\phi_{pseudo} = BV \quad (7)$$

where B is the coefficient matrix. For specific pseudo-baseline combination thresholds and sensor parameters, matrix B is fixed. Thus, the unknown matrix A can be solved directly using the least squares method. Considering the potential ill-conditioned problem of the function [35], ridge estimation was introduced in this study to ensure the robustness of the deformation estimations.

3. Performance Verification

In this section, deformations were estimated using simulated data and real data from Sentinel-1 covering Beijing to assess the performance of the pseudo-combination SBAS algorithm.

3.1. Performance Verification Using Simulated Data

Since the phase components in the interferometric phase are complex, the residual topography phase may be mixed with the atmosphere phase and thermal noise phase, which increases the complexity of the performance verification of the pseudo-combination SBAS algorithm. Data simulations can control each phase component in the interferograms, which makes them effective for testing the algorithm. In this subsection, a set of simulation

interferograms were constructed based on the simulated deformation and DEM residuals. Note that, other noise such as atmospheric noise and thermal noise was not included in the simulated data in order to verify the performance of the algorithm in separating deformation phase and terrain error phase.

The simulated deformation data were constructed using Kriging interpolation in ArcGIS, and a deformation field with a maximum settlement of 10 mm/year was generated (Figure 2a). In terms of DEM residual simulation, since the calculation of each pixel in the pseudo-combination SBAS algorithm is independent, the distribution of residual DEM does not affect the estimation accuracy [28]. To make the simulated data more realistic, the SRTM [39] and ASTER GDEM [40] DEM data covering the same area were acquired and the differences between the two DEM datasets were calculated (Figure 2b). The height of the simulated DEM residual map ranged from -94 m to 107 m.

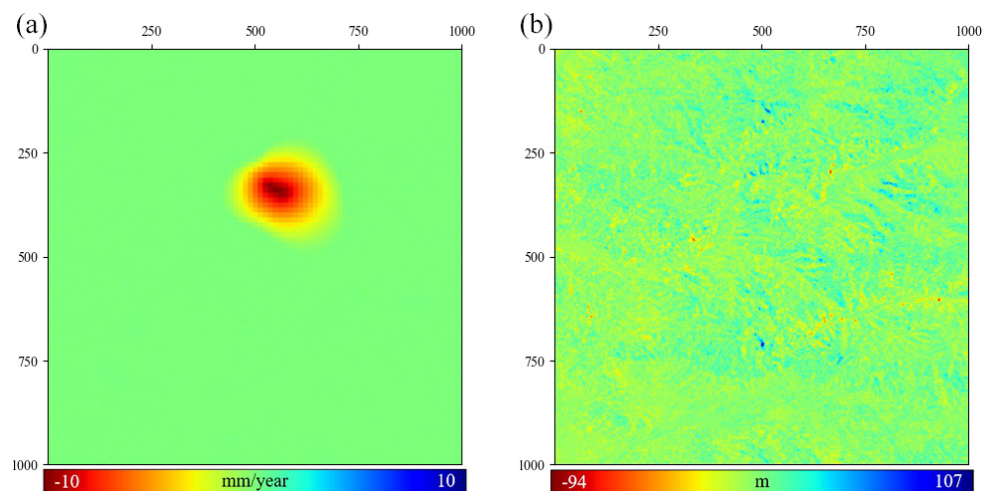


Figure 2. Simulated data. (a) Simulated deformation data and (b) simulated DEM residual error data.

Additional satellite sensor parameters (e.g., incident angle and baseline) were required to construct the simulated differential interferograms. In this study, parameters from a Sentinel-1 dataset covering Beijing, China, were introduced. This Sentinel-1 dataset contained 28 scenes spanning from May 2017 to May 2018. With a 50-day temporal baseline threshold and a 150 m spatial baseline threshold, 92 differential interferograms were constructed. The spatial-temporal baselines of the interferograms are illustrated in Figure 3, where the maximum perpendicular baseline is 146 m.

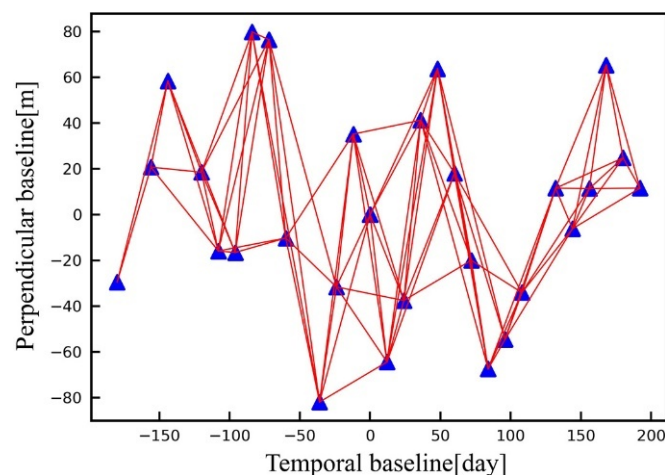


Figure 3. Temporal and perpendicular baselines of Sentinel-1 data.

Based on the 92 simulated interferograms, 90 pseudo-baseline combinations were generated using a 2 m pseudo-baseline threshold. Subsequently, the combined interferograms were processed by the pseudo-combination SBAS algorithm, and the estimated deformation field (Figure 4e) was obtained. The results show that the artifact related to residual DEM was effectively mitigated by this approach. The maximum difference between the simulated deformation field (Figure 4a) and the calculated deformation field (Figure 4e) was approximately 0.3 mm/year, and the standard deviation of the difference was approximately 0.02 mm/year.

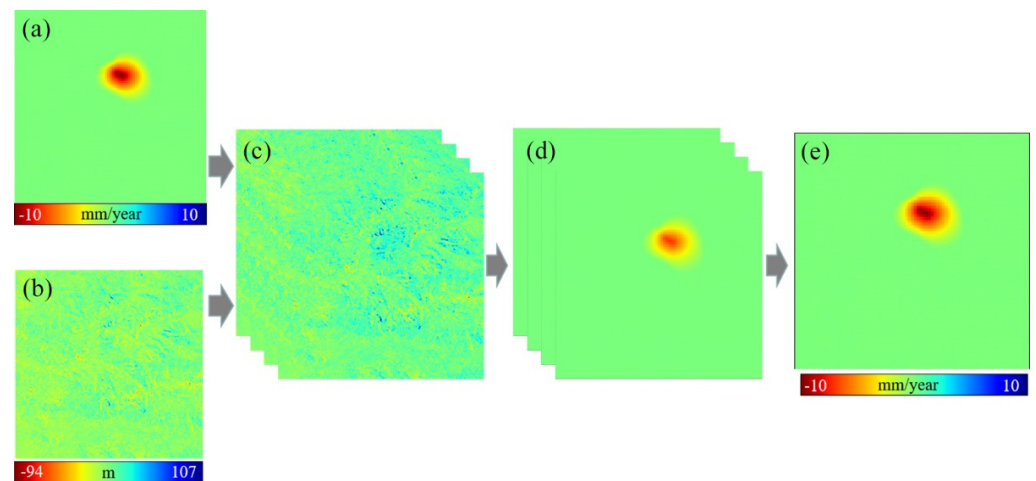


Figure 4. Pseudo-combination SBAS deformation calculation. (a) Simulated deformation data; (b) simulated height data; (c) simulated differential interferogram; (d) pseudo-combination of interferogram; and (e) deformation calculation result.

To further verify the performance of the pseudo-combination SBAS algorithm, a classic SBAS algorithm [32] was used to process the simulated data for comparison. The SBAS algorithm was executed twice in this study: in the first implementation the residual topography was ignored, while in the second implementation it was modeled as a parameter of SBAS. The results of the two deformation solutions are shown in Figure 5a,b. The deformation time series of a typical point (point of interest, POI), marked by a red circle, is shown in Figure 5d, which was known to be stable with a deformation equal to 0 during the study period. The linear deformation result of the first implementation shows an obvious terrain-related artifact, and the deformation time series of the POI showed an oscillatory error, which was caused by the residual topography error and could lead to a maximum error of -5.2 mm/year. Furthermore, the second implementation showed little improvement over the first in this study; the estimated deformation rate at the POI was only 0.3 mm/year lower than that without a DEM estimation, which may be attributed to the short perpendicular baselines of Sentinel-1 data. In contrast, the residual DEM-related error was effectively mitigated in the deformation field estimated by the pseudo-combination SBAS algorithm. The deformation time series calculated by the proposed pseudo-combination method was close to zero during the whole period, and the estimated linear deformation at the POI was about -0.18 mm/year, which is close to the input deformation value (0 mm/year).

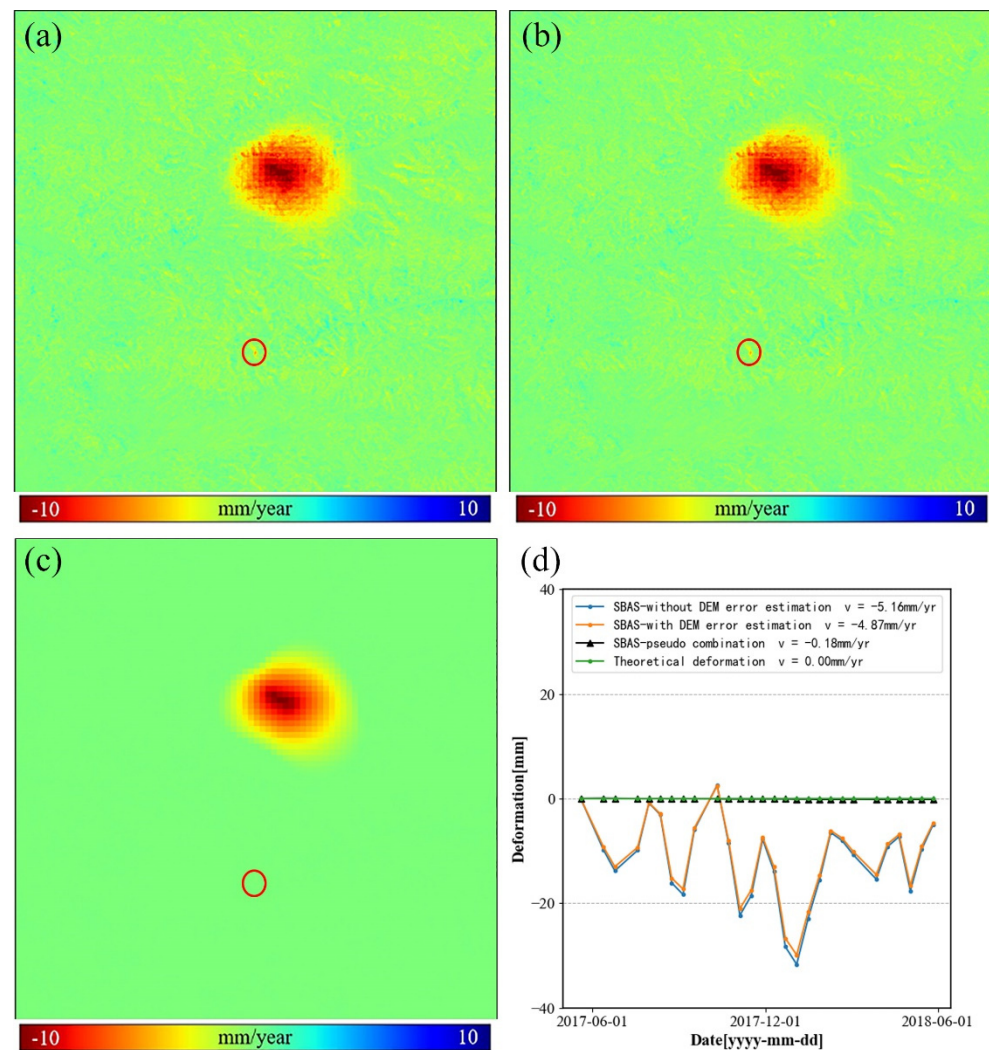


Figure 5. The deformation estimations calculated by different algorithms. (a) Deformation field calculated by SBAS (without DEM error estimation); (b) deformation field calculated by SBAS (with DEM error estimation); (c) deformation field calculated by pseudo-combination SBAS; and (d) the deformation time series calculated by different algorithms.

The deformation fields time series derived from the SBAS (with DEM estimation) and pseudo-combination SBAS algorithms are shown in Figures 6 and 7, respectively. In the deformation results from the SBAS algorithm, the deformation fields over different time intervals were disturbed by DEM residual signals to varying degrees. The maximum deformation error generated by the terrain noise reached 29.9 mm, which would interfere with the interpretation of deformation results. In contrast, the deformation fields derived from the pseudo-combination SBAS algorithm were free of terrain-related artifacts in all time intervals, and the maximum deformation error caused by DEM residuals was 0.5 mm. It is worth noting that although the simulation tests were carried out using data from Sentinel-1, the proposed pseudo-combination SBAS algorithm was also effective for other SAR data such as TerraSAR-X.

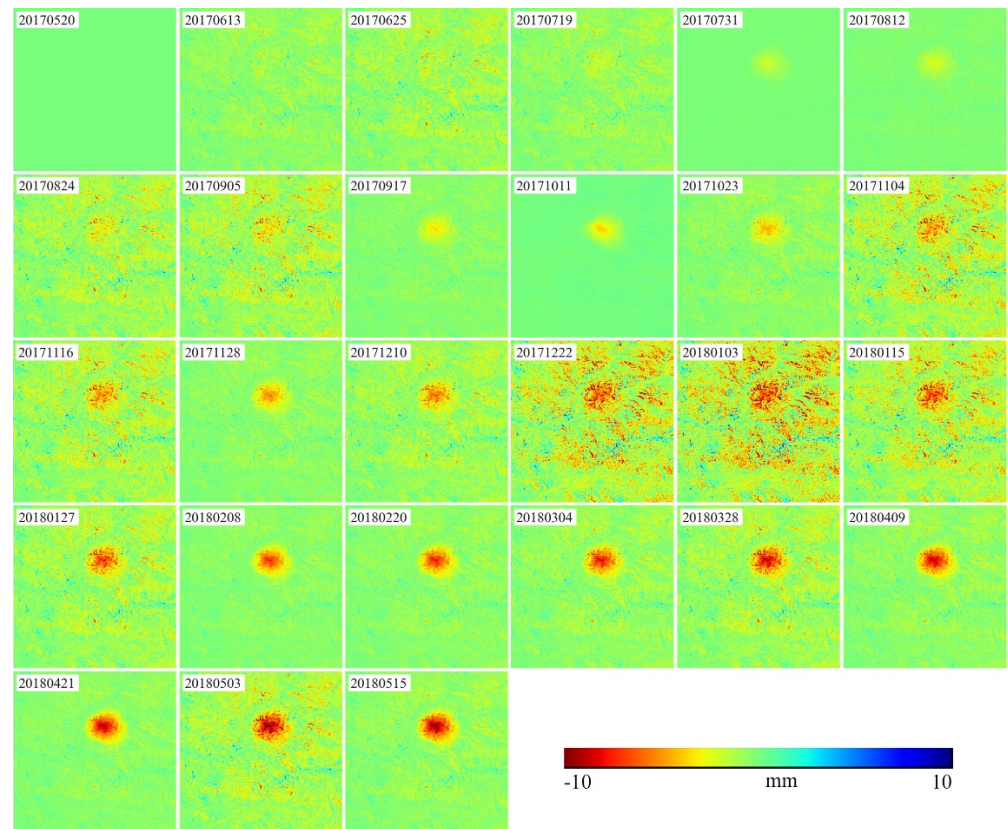


Figure 6. Time series deformation fields calculated by the SBAS algorithm.

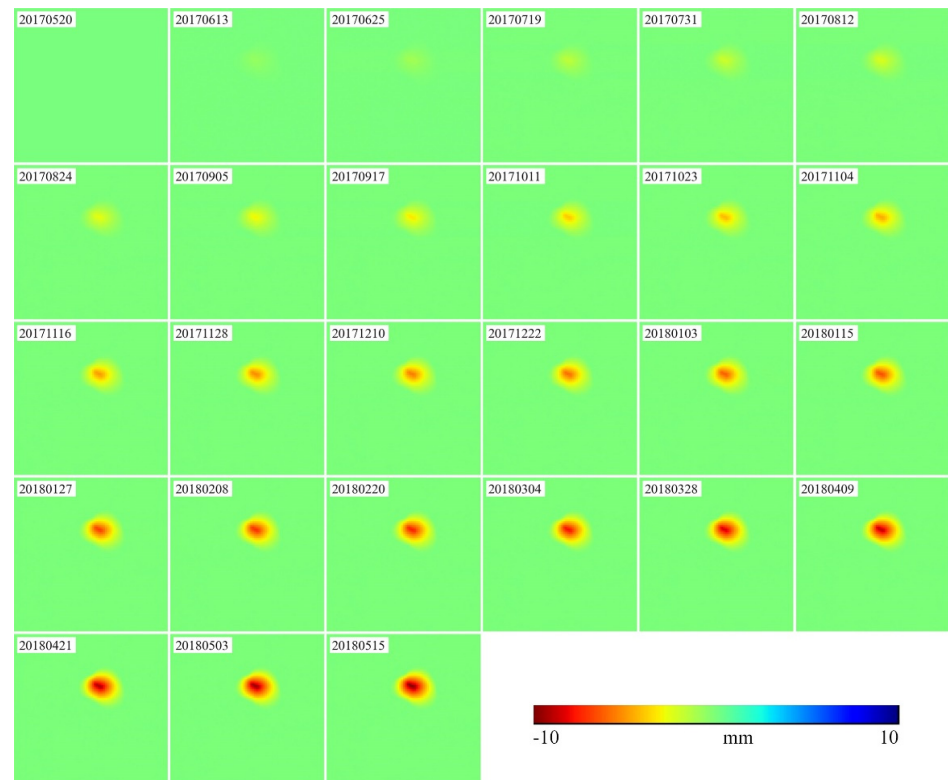


Figure 7. Time series deformation fields calculated by the pseudo-combination SBAS algorithm.

3.2. Performance Verification on Real Data

Compared with the simulated data, the phase composition in the real interferogram was more complex and included incoherent noise, atmospheric phase, unwrapping error, etc. This makes it especially necessary to further verify the performance of the pseudo-combination SBAS algorithm using real data. The land subsidence in Beijing is typical and has been studied for years [41–43]. Thus, Beijing was selected as a test area, and the SBAS algorithm and the pseudo-combination SBAS algorithm were both implemented based on a set of Sentinel-1 images covering Beijing.

The Sentinel-1 dataset consisted of 28 scenes acquired from May 2017 to May 2018. After image coregistration and the other preprocessing steps, 92 interferograms were generated using a 150 m spatial baseline threshold and a 50-day temporal baseline threshold. The spatio-temporal baseline distribution of the interferograms is illustrated in Figure 3. Subsequently, SRTM data were introduced to differentiate the topography phase, and a multilook factor of 10 (in range):2 (in azimuth) was applied for smoothing the differential interferograms. In addition, the reference phase area was Tiananmen Square, for which the SAR images were properly cropped (11,000 columns in range and 5000 rows in the azimuth direction) in advance to improve the efficiency of data processing.

The SBAS and pseudo-combination SBAS algorithms were both applied to the Sentinel-1 data covering Beijing, and the corresponding deformation results are shown in Figure 8a,b, respectively. It was obvious that the deformation fields detected by the two algorithms were highly consistent and that the settlement pattern was consistent with the settlement results obtained by Zhou et al. [44], which were derived using the Tomo-PSInSAR algorithm. The above qualitative analysis provided a preliminary verification of the consistency of the SBAS pseudo-baseline combination algorithm and the SBAS algorithm in detecting settlement in a plain area.

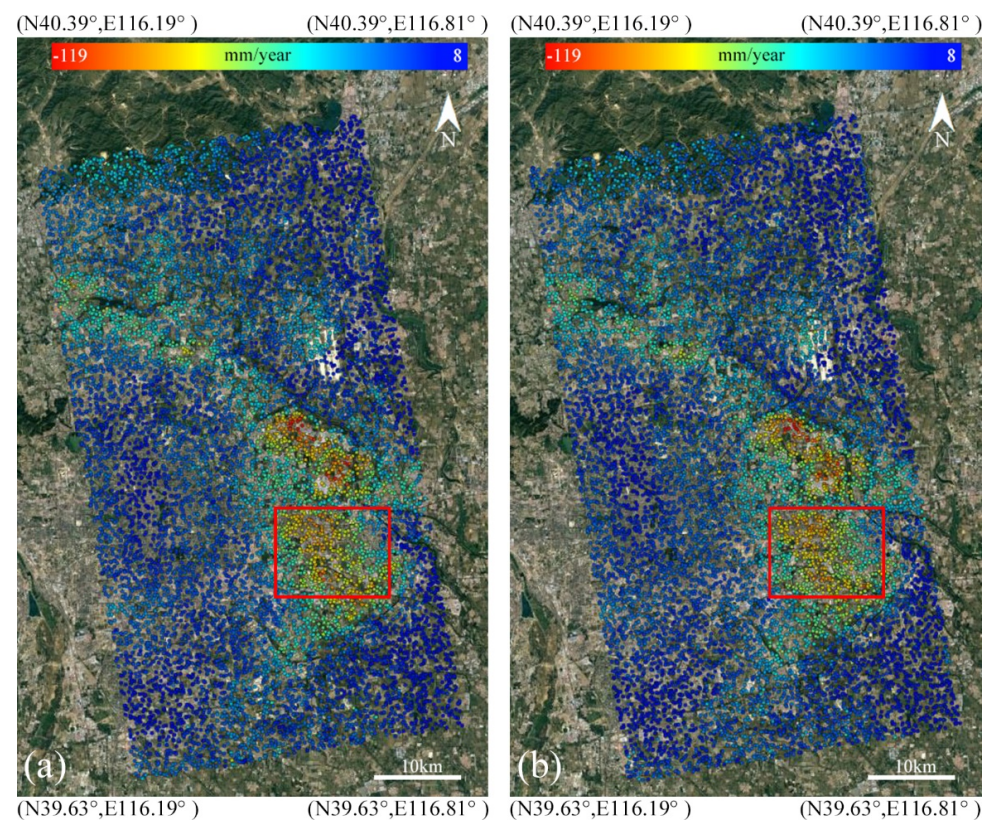


Figure 8. The deformation fields of Beijing calculated by different algorithms. (a) Deformation field calculated by the SBAS algorithm; and (b) deformation field calculated by the pseudo-combination SBAS algorithm.

To quantitatively analyze the deformation results derived from the two different algorithms, the deformation fields of a subregion (rectangles in Figure 8) was clipped from Figure 8, and the deformation rates of the two algorithms were compared (Figure 9). The deformation rates ranged from -10 to 120 mm/year during the SAR observation period, and the correlation coefficient between the two measurements was 0.994 . In addition, the deformation information time series of three typical points (P1, P2, and P3 in Figure 9a) are illustrated in Figure 9d, wherein the deformation time series of the two algorithms can also be seen to be in agreement. The precise position of the settlement funnel and the high consistency between the two calculations demonstrated the reliability of the pseudo-combination SBAS algorithm in a plain area.

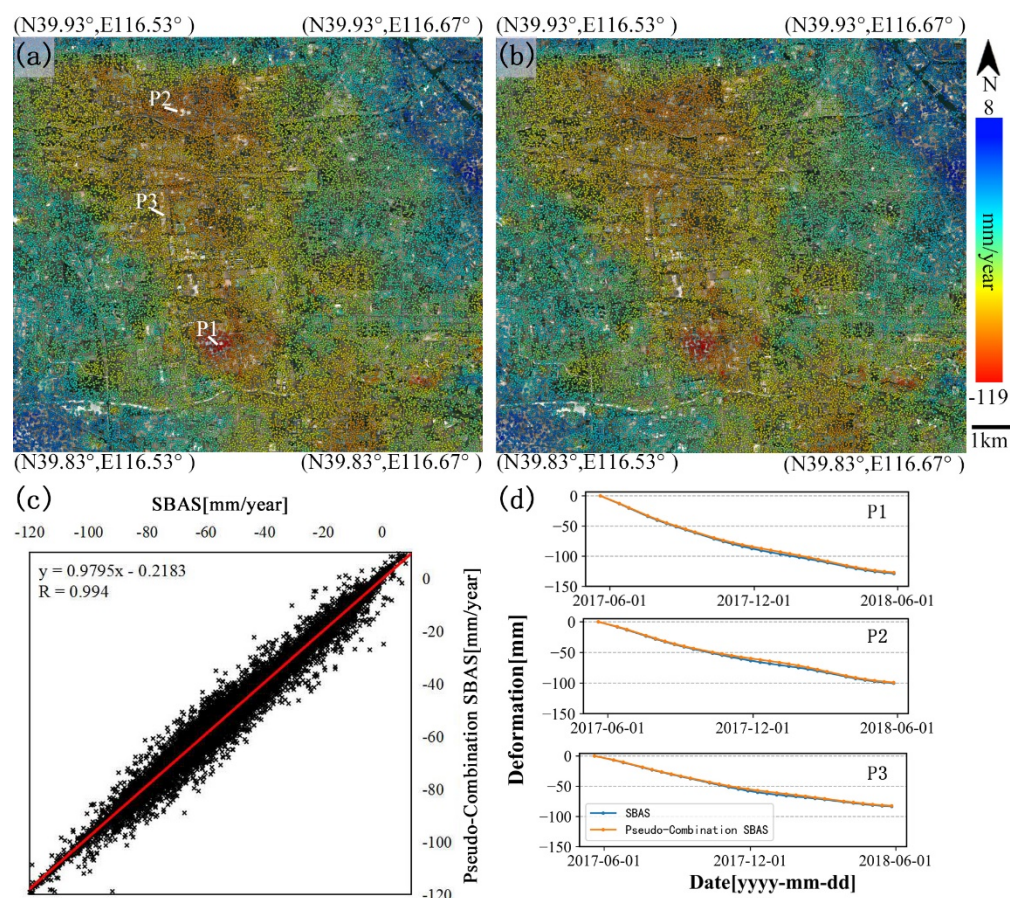


Figure 9. Algorithm performance verification. (a) Deformation field calculated by the SBAS algorithm; (b) deformation field calculated by the pseudo-combination SBAS algorithm; (c) scatter plot of the results of the SBAS and pseudo-combination SBAS algorithms; and (d) comparisons of deformation time series at three points.

4. Application to Mountain Area

4.1. Study Site

The Great Wall was designated a world cultural heritage site in 1987 due to its irreplaceable cultural and historical value [45]. However, long-term natural erosion and anthropogenic activities have imposed challenges to the maintenance and sustainable development of the Great Wall [46–48], and the condition of the Great Wall shows high spatial heterogeneity due to the differences in construction materials and driving forces along the long span of its heritage [25]. In this study, a representative section of the Great Wall located in Shanhaiguan City and its surroundings were investigated with the InSAR technique to locate any deformation anomalies in the landscape surrounding this heritage site.

The 27 km-long Shanhaiguan section of the Great Wall is the start of the Ming Great Wall and is located to the northeast of Qinghuangdao City, Hebei Province [11]. This section

of the Great Wall can be taken as representative of the Ming Great Wall and can be divided into mountain, plain, and coastal sections according to the terrain features. However, the Shanhaiguan section of the Great Wall is seriously damaged, and its foundation is sinking, causing cracking in the wall [49], and some parts of the wall have even collapsed (Figure 10).



Figure 10. On-site photos of the Shanhaiguan section of the Great Wall.

4.2. Data

A descending C-band Sentinel-1 dataset (51 scenes) in Terrain Observation with Progressive Scan (TOPS) mode was collected from October 2016 to August 2018 and applied to measure deformation in the research area. The central incidence angle of the SAR imaging was 39.3° , and the range and azimuth pixel spacing of the SAR dataset were approximately 2.33 m and 13.95 m, respectively. The coverage of the SAR data is shown in Figure 11a by the yellow rectangle, and the study area clipped from the SAR images is highlighted by the red rectangle. The spatio-temporal baseline of the data is shown in Figure 12.

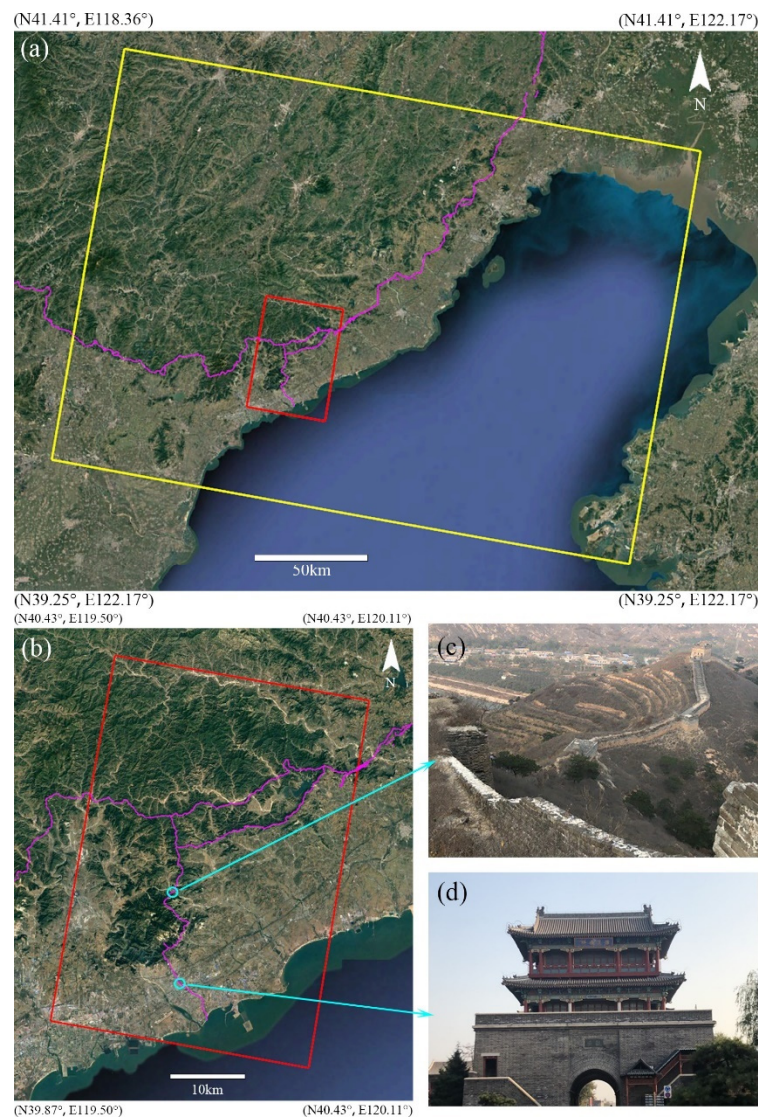


Figure 11. Overview of the study area. (a) Coverage of Sentinel-1 dataset (yellow rectangle) and the clipped area (red rectangle). The purple lines indicate the path of the Great Wall; (b) Coverage of the clipped area; and (c,d) two typical landscapes within the research area.

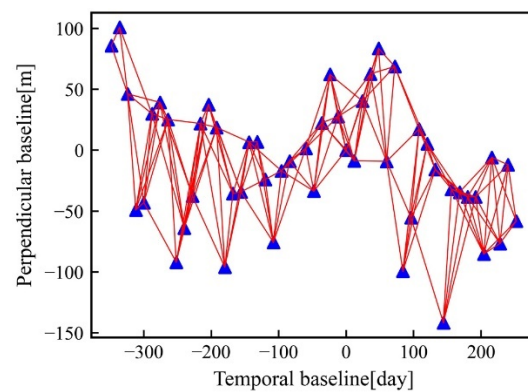


Figure 12. Temporal and perpendicular baselines of Sentinel-1 data.

4.3. Data Processing

Before the deformation inversion of InSAR, the SAR images needed to be pre-processed via image coregistration, cropping, small baseline subset selection, and differential

interferogram generation. In this study, the SAR images were coregistered using the amplitude correlation method [50], which achieves an accuracy better than 1/10 of a pixel and avoids any decorrelation caused by coregistration errors. Subsequently, the SAR images were cropped to improve processing efficiency and a subgraph covering the research area (3500 rows in azimuth and 9500 columns in range) was generated (red rectangle in Figure 11a). Then, a 120 m spatial baseline threshold and a 50-day temporal baseline threshold were applied to select the interferograms with small baselines. Finally, 165 interferograms that met the restriction of coherence threshold were generated (Figure 12). Next, the multilooking, filtering, and unwrapping processes were implemented on the generated interferograms. It is worth noting that terrain-related atmospheric noise in large-scale mountainous areas cannot be ignored. Thus, an atmospheric correction technology was applied to the unwrapped interferograms [51].

Based on the unwrapped interferograms, the SBAS and pseudo-combination SBAS algorithms were applied to characterize the deformation field of the research area. For SBAS processing, an average coherence coefficient threshold of 0.2 was used as the threshold to mask uncoherent points, and a coherence point located in the southern part of the research area was selected as the reference point (pink pentagram mark in Figure 13a). Based on the parameters of the SBAS algorithm, a 3 m vertical baseline combination threshold was used for the pseudo-combination SBAS processing, and 283 pseudo-baseline combined interferograms were obtained. The deformation fields obtained by SBAS and pseudo-combination SBAS algorithms are shown in Figure 13a,b.

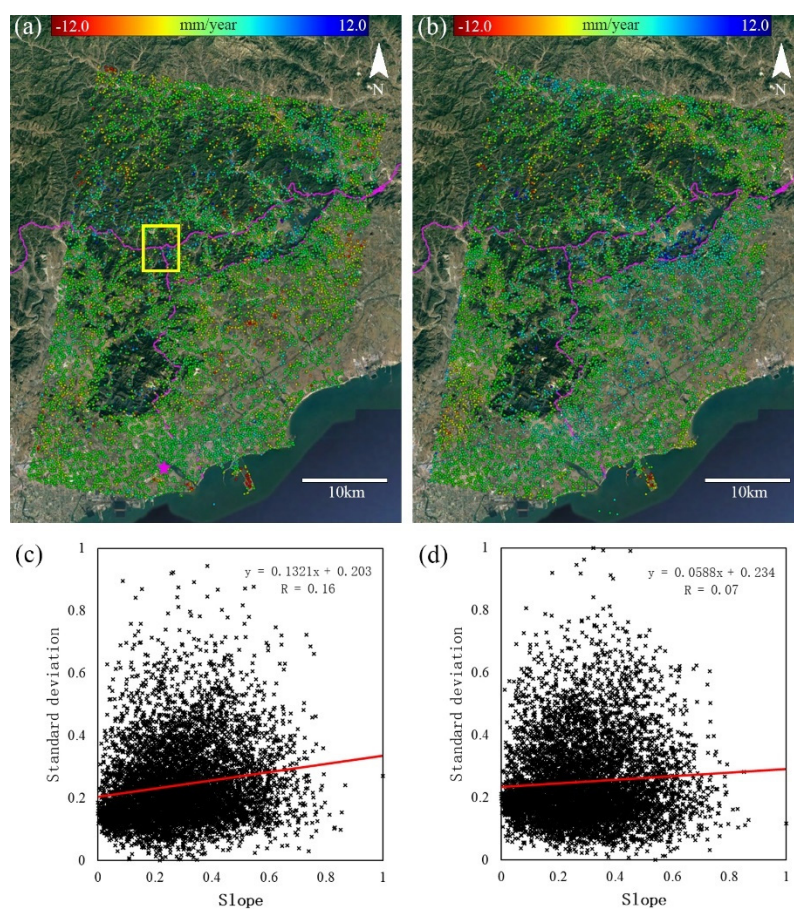


Figure 13. The deformation fields of Shanhaiguan calculated by different algorithms. (a) Deformation field calculated by the SBAS algorithm; (b) deformation field calculated by the pseudo-combination SBAS algorithm; and (c,d) scatter plots for the slopes and standard deviation of the respective algorithms.

4.4. Deformation Interpretation

In this study, due to the lack of high-precision elevation data for the Shanhaiguan area, the error of the external DEM (SRTM) could not be determined, so the performance of the pseudo-combination SBAS algorithm could not be directly verified. Nevertheless, the errors in the SRTM data were correlated with the surface slopes [38,52], with higher surface slopes resulting in higher absolute values of SRTM error, resulting in a slope-related error in the deformation time series of the InSAR results. Thus, the performance of the pseudo-combination SBAS algorithm in the Shanhaiguan research area was evaluated based on the correlation between the surface slope and the standard deviation of the InSAR time series results.

Specifically, the surface slope and standard deviation of the deformation were compared at each coherence point within the yellow rectangle (mountainous area) in Figure 13a, and two scatter plots were generated (Figure 13c,d). Because the standard deviations and surface slopes were inconsistent, their values were normalized in advance. According to the scatter plot of the SBAS algorithm (Figure 13c), there was an obvious correlation between the slope and the standard deviation values. With increasing slope, the standard deviation of the deformation time series tended to increase gradually, and the correlation coefficient (r) was 0.16. However, the correlation coefficient in the scatter plot of the pseudo-combination SBAS algorithm was only 0.07 (Figure 13d). Furthermore, the mean value of the standard deviation decreased from 3.69 mm in SBAS to 2.36 mm in the pseudo-combination SBAS algorithm. The decrease in the correlation coefficient and the mean value of the standard deviation verified the effectiveness of the pseudo-combination SBAS algorithm in the removal of elevation residuals in mountainous areas.

Since the motion velocity distribution of the pseudo-combination SBAS could be considered normal distribution at all points (Figure 14), the “Standard Deviation Classification method” was used to classify the points as stable and unstable. This classification method finds the mean value of the observations, then classify the data by the defined standard deviation, which is a commonly used tool in ArcGIS software (<https://www.esri.com/en-us/arcgis/about-arcgis/> (accessed on 10 October 2021)). Specifically, the points with motion velocity greater than 1 standard deviation (8.3 mm/year) were considered as unstable points, while the other points were considered as stable, since their deformation was too small to be detected by our InSAR method. Next, a 500 m buffer along the Great Wall was generated to evaluate the stability of the Shanhaiguan Great Wall corridor, and a thematic stability map of Shanhaiguan Great Wall corridor was obtained (Figure 15). The plain section of the Great Wall corridor in the southeast of the study area maintained high stability during the InSAR monitoring period. In contrast, local deformation anomalies were detected in the mountainous areas in the central and northern parts of the Great Wall corridor. According to the field investigation, although the plain section of the Great Wall in the southeast passes through the urban area of the city of Shanhaiguan, it has been preserved by the local government during the urban construction process; thus, it has not been significantly disturbed by human activities. In the central and northern areas of the study area, the mountainous areas, the Great Wall was assembled using stones, which are prone to falling off or collapsing due to the combined effects of the mountain slope and natural erosion.

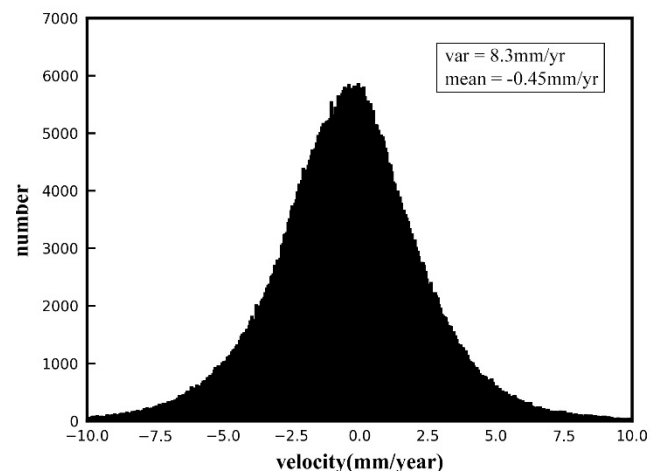


Figure 14. Motion velocity distribution of the pseudo-combination SBAS.

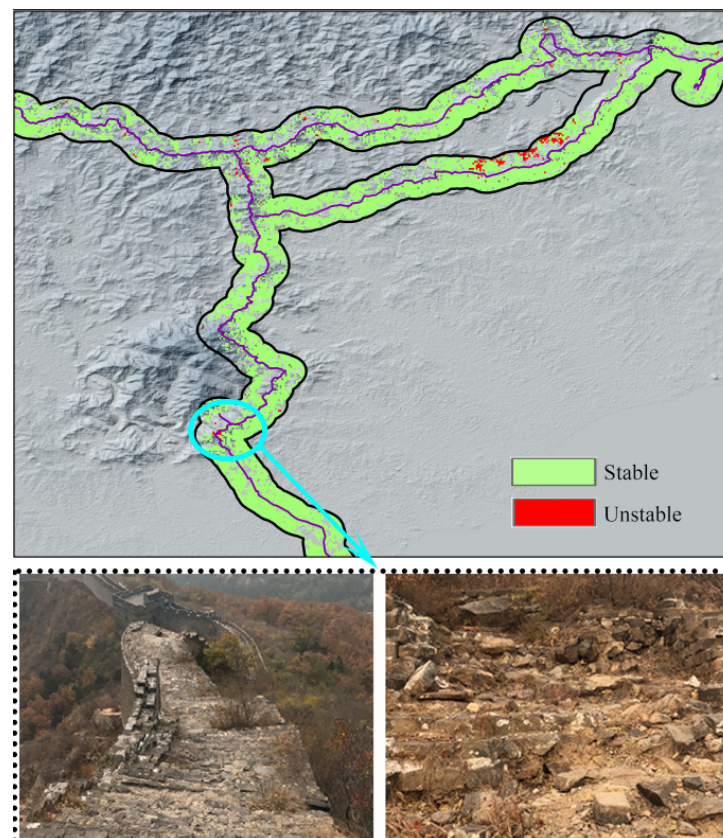


Figure 15. Thematic map of the stability of the Shanhaiguan Great Wall corridor (top) with two typical landscapes in the unstable area (bottom).

5. Discussion

The above experimental results have demonstrated the advantages of the proposed pseudo-combination SBAS method, which can effectively reduce the residual topography effect introduced by the inaccurate external DEM in a mountainous area. This section focuses on the discussion of the improvements and limitations of the proposed method.

This study adopted the idea of pseudo-baseline combination proposed by Zhang et al. [35], but the application scenarios of the two algorithms are quite different: Zhang's method mainly solves the elevation underestimation problem in urban areas based on TCP-InSAR, while the SBAS pseudo-baseline combined algorithm developed from the SBAS method is

not sensitive to the height of single buildings due to multilooking and filtering processing, and it is more applicable to deformation monitoring in large-scale mountainous areas.

Compared with the method proposed by Zhang et al. [35], the interferograms were unwrapped before the pseudo-baseline combination. Since the decorrelation noise of InSAR is additive, the double combination of interferogram will increase the noise, which means the noise level of the pseudo-combination interferogram will always be higher than that of the two input interferograms (Figure 16). Unwrapping is one of most complicated steps in InSAR processing, and it is sensitive to the noise level of the input interferogram. Therefore, we chose to unwrap the interferograms before the double combination of the interferograms to mitigate unwrapping error, which further improved the accuracy of the pseudo-combination SBAS result.

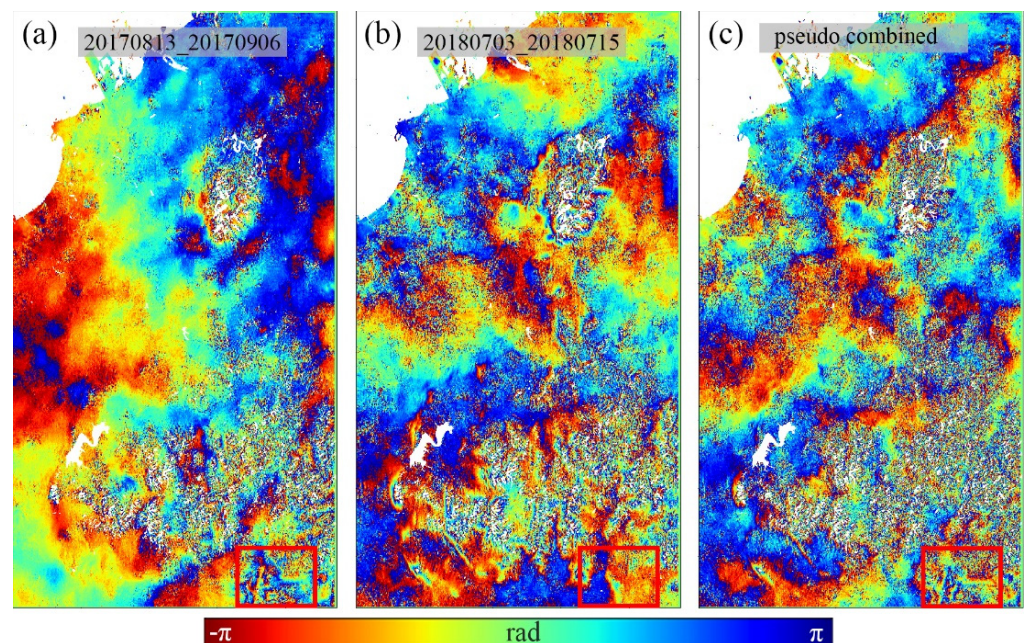


Figure 16. Example of noise propagation. (a,b) The two original interferograms with different time spans and (c) the pseudo-combined interferogram of the previous two images. The red rectangle shows the typical noise propagation phenomenon.

On the other hand, the pseudo-combination SBAS method proposed in this study still had certain limitations that may affect the construction and interpretation of the derived deformation. The first limitation was the absence of InSAR measurements for vegetated areas. This means that the measurement density of the pseudo-combination SBAS method is still limited throughout mountainous areas. Parts of the region in the study area may have suffered from serious temporal decorrelations due to the growth of vegetation, resulting in blank areas in the InSAR measurements. As illustrated by the red circles in Figure 17, there were clear gaps in the InSAR measurements along the Great Wall. Thus, a more flexible point selection algorithm should be introduced to increase the point density in mountainous areas. Furthermore, since the InSAR method may fail in densely vegetated areas, it may be possible to apply optical remote sensing methods to complement the InSAR measurements and enable comprehensive deformation monitoring along the Great Wall corridor.

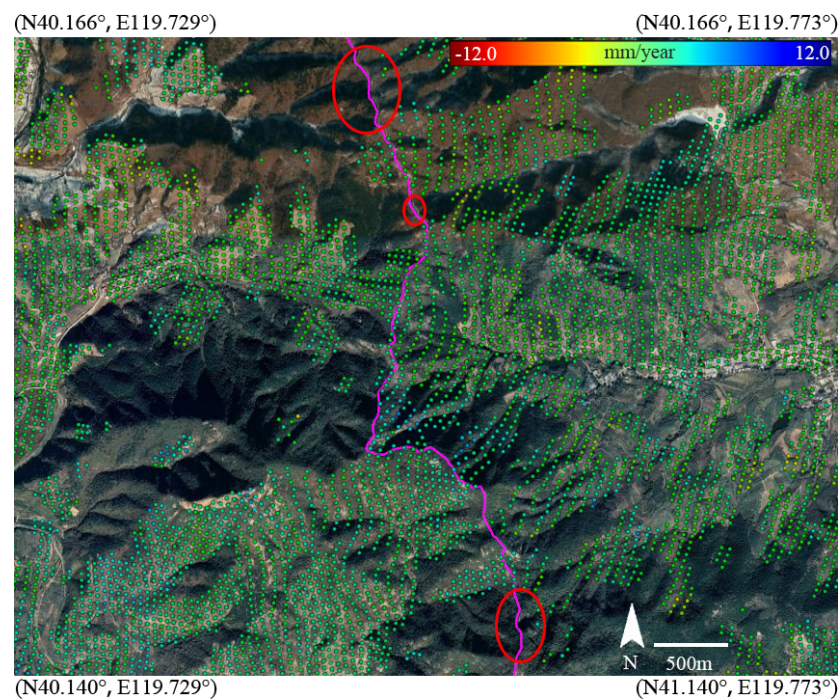


Figure 17. Distribution of InSAR measurements; red circles indicate areas with gaps in the InSAR measurements along the Great Wall. The purple line indicates the location of the Great Wall.

The second limitation was that the spatial resolution of the applied Sentinel-1 data was relatively coarse. The original spatial resolution of the Sentinel-1 data was approximately 5 m in the range direction and 20 m in the azimuth direction, but the resolution became even coarser after the multilooking and filtering processes (i.e., 50 m in the range direction and 40 m in the azimuth direction), which made it unsuitable for monitoring structural deformation of the Great Wall itself. Thus, this study only monitored the stability of the landscape surrounding the Great Wall corridor. However, when protecting architecture heritage structures, we should not be limited to monitoring the surrounding landscape and should utilize datasets that allow monitoring of the heritage sites themselves. Therefore, SAR data with a higher resolution (i.e., TerraSAR-X data in Spotlight mode) should be applied to acquire more detailed structural deformation monitoring of the Great Wall to facilitate adaptive protection of this heritage site. Specifically, in the following work, hotspots along the Great Wall with motion anomalous will first be identified using the Sentinel-1 data with the proposed pseudo-combination SBAS method. The detected hotspots will be further investigated with the high-resolution TerraSAR-X data.

The third limitation was that atmospheric noise was amplified in the pseudo-combined interferograms. The double combination process for generating interferograms can increase the noise levels of the phase images [35]. Figure 18 shows the atmospheric-related noise did accumulate in the combined images. To address this, a linear fitting algorithm [51] was applied to mitigate the atmospheric-related noise within the interferogram. As illustrated in Figure 19, the linear trends in atmospheric phase and the topography-correlated atmospheric phase were mitigated in the interferograms. However, the spatially varying turbulence atmospheric phase was not fully resolved in this study (Figure 18a), and this noise signal was amplified in the pseudo-combined interferograms (Figure 18c), which may have affected the stability of the InSAR solution. Therefore, the noise level, especially the turbulence atmospheric phase, should be carefully considered to improve the pseudo-combination SBAS method in subsequent studies.

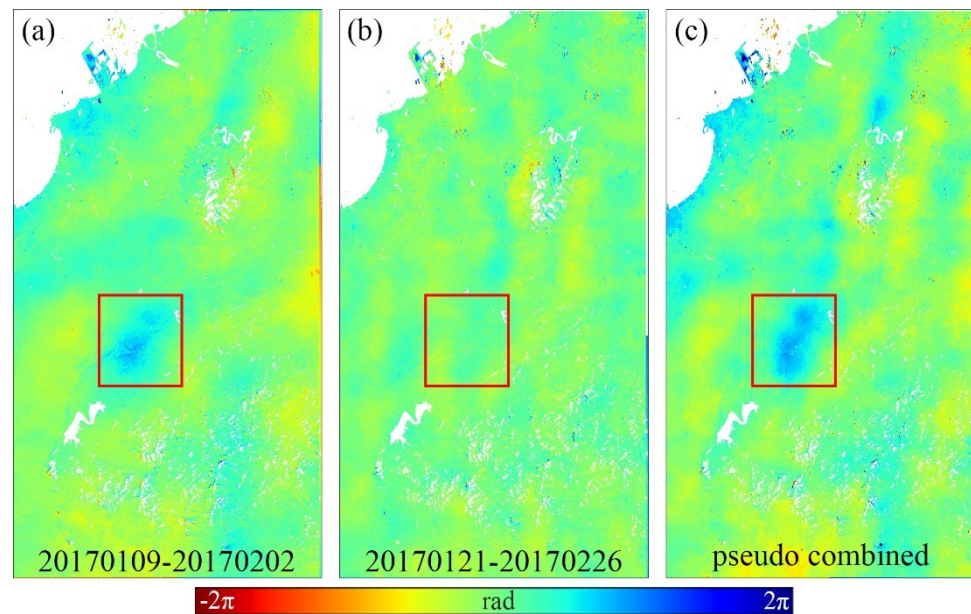


Figure 18. Example of the turbulence atmospheric effect. (a,b) The two original interferograms with different time spans; and (c) the pseudo-combined interferogram of the previous two images.

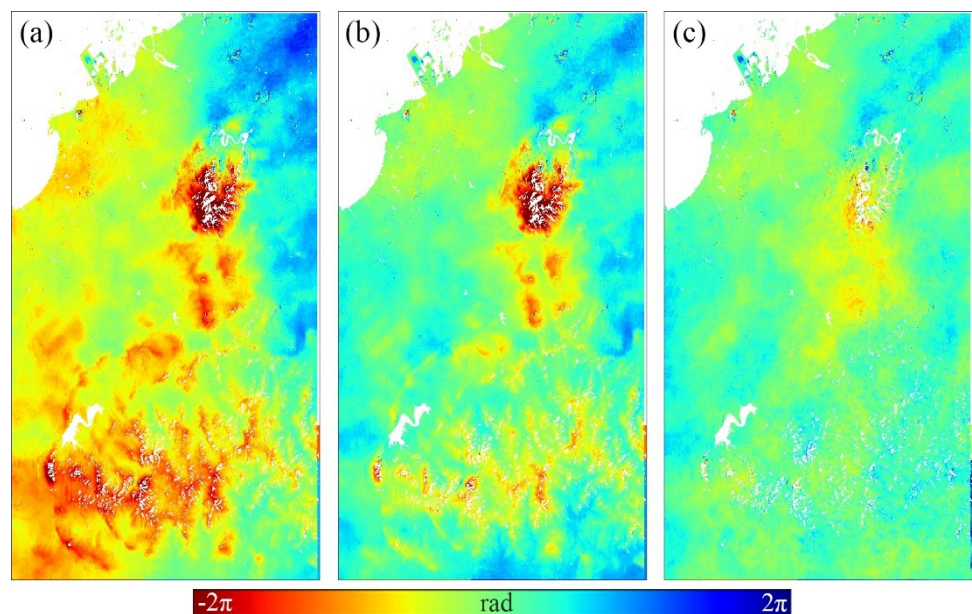


Figure 19. Example of atmospheric noise mitigation. (a) Original interferogram (27 April 2017–21 May 2017); (b) interferogram after linear detrending; and (c) interferogram after topography-correlated atmospheric phase correction.

6. Conclusions and Prospects

In this study, the SBAS approach was improved by adopting the pseudo-baseline combination strategy to avoid estimation errors linked to the usage of inaccurate digital elevation models (DEM), and an MTInSAR algorithm suitable for a complex terrain environment was proposed.

Firstly, the effectiveness of the proposed algorithm was sequentially tested using a simulated dataset and a real dataset consisting of 28 scenes from Sentinel-1 images covering Beijing. In the experiments using simulated data, the maximum deformation velocity error and maximum deformation error were 5.2 mm/year and 29.9 mm, respectively, while the corresponding errors in the pseudo-combination SBAS results were only 0.3 mm/year and

0.5 mm. In the experiment using real data from the Beijing area, the motion rates obtained by the SBAS and pseudo-combination SBAS algorithms were consistent, and the correlation coefficient between the two deformation velocities was as high as 0.994. Subsequently, the verified pseudo-combination SBAS algorithm was applied to the Shanhaiguan section of the Great Wall and its surroundings, and a thematic map was generated to show the stability of the landscape of the Great Wall corridor. The deformation calculation results reveal that the landscape around the Shanhaiguan section of the Great Wall was generally stable, but local instabilities were detected in some mountainous areas. Combined with the field investigation, the deformation anomalies may have been related to the distributed, unstable rock in the mountainous area.

This study revealed the potential of the proposed pseudo-combination SBAS algorithm in stability monitoring and risk assessment of the landscape of architectural heritage sites in mountainous areas. In future research, we will focus on overcoming the limitations of the pseudo-combination SBAS algorithm and improving its adaptability in deformation monitoring in mountainous areas by taking the following measures: First, Sentinel-1 data will be incorporated with other high-resolution SAR data [53–55] to facilitate a coarse to fine deformation monitoring strategy for the detailed motion monitoring of heritage sites on complex topography; Then, in order to optimize the method, the coherent scatterers (CS)-based InSAR algorithm [56,57] will be introduced to improve the density of InSAR measurements in mountainous areas; thereafter, a more comprehensive atmospheric correction strategy (e.g., GAOCs method [58] and spatially variable power law method [59]) will be applied to deal with local microclimate effects (turbulence) to complement the modeling-based atmospheric correction method used in this study.

Author Contributions: Conceptualization, F.C. and H.X.; methodology, F.C. and H.X.; software, C.W.; validation, H.X., W.Z. and C.W.; formal analysis, H.X.; investigation, H.X. and C.W.; resources, F.C. and W.Z.; data curation, W.Z.; writing—original draft preparation, H.X. and F.C.; writing—review and editing, H.X. and F.C.; visualization, H.X. and C.W.; supervision, F.C.; project administration, W.Z.; funding acquisition, F.C. All authors have read and agreed to the published version of the manuscript.

Funding: This research was supported by the National Key Research and Development Program of China (Grant No. 2017YFE0134400).

Institutional Review Board Statement: Not applicable.

Informed Consent Statement: Not applicable.

Data Availability Statement: The data presented in this study are available on request from the corresponding author.

Acknowledgments: The authors thank Lei Zhang for sharing his helpful experience in InSAR data processing. The Sentinel-1A data of Beijing and Qinghuangdao Cities were downloaded from the Sentinel-1 Scientific Data Hub.

Conflicts of Interest: The authors declare no conflict of interest.

References

1. Gibas-Tracy, D.R. Cost-effective environmental consulting using geographic information systems and remote sensing. *Geoscience and Remote Sensing Symposium*, 1996. *Int. Geosci. Remote Sens. Symp.* **1996**, *4*, 2234–2236. [[CrossRef](#)]
2. Crosse, W. The opportunities and constraints in using cost-effective satellite remote sensing for biodiversity monitoring. *Oceans IEEE* **2005**, *1*, 844–849. [[CrossRef](#)]
3. Shinozuka, M.; Ghanem, R.; Houshmand, B.; Mansouri, B. Damage detection in urban areas by SAR imagery. *J. Eng. Mech.* **2000**, *126*, 769–777. [[CrossRef](#)]
4. Ma, M.; Chen, J.; Liu, W.; Yang, W. Ship classification and detection based on CNN using GF-3 SAR images. *Remote Sens.* **2018**, *10*, 2043. [[CrossRef](#)]
5. Bamler, R.; Hartl, P. Synthetic aperture radar interferometry. *Inverse Probl.* **1998**, *14*, R1–R54. [[CrossRef](#)]
6. Jiang, Y.; Xu, Q.; Lu, Z. Landslide Displacement Monitoring by Time Series InSAR Combining PS and DS Targets. *Int. Geosci. Remote Sens. Symp.* **2020**, 1011–1014. [[CrossRef](#)]
7. Horst, T.; Rutten, M.M.; Giesen, N.C.; Hanssen, R.F. Monitoring land subsidence in Yanggon, Myanmar using Sentinel-1 persistent scatterer interferometry and assessment of driving mechanisms. *Remote Sens. Environ.* **2018**, *217*, 101–110. [[CrossRef](#)]

8. Milillo, P.; Perissin, D.; Salzer, J.T.; Lundgren, P.; Lacava, G.; Milillo, G.; Serio, C. Monitoring dam structural health from space: Insights from novel InSAR techniques and multi-parametric modeling applied to the Pertusillo dam Basilicata, Italy. *Int. J. Appl. Earth Obs. Geoinf.* **2016**, *52*, 221–229. [[CrossRef](#)]
9. Crosetto, M.; Monserrat, O.; Cuevas-Gonzalez, M.; Cuevas-González, M.; Devanthérya, N.; Luzia, G.; Crippab, B. Measuring thermal expansion using X-band persistent scatterer interferometry. *ISPRS J. Photogramm. Remote Sens.* **2015**, *100*, 84–91. [[CrossRef](#)]
10. Qin, X.; Li, Q.; Ding, X.; Xie, L.; Wang, C.; Liao, M.; Zhang, L.; Zhang, B.; Xiong, S. A structure knowledge-synthetic aperture radar interferometry integration method for high-precision deformation monitoring and risk identification of sea-crossing bridges. *Int. J. Appl. Earth Obs. Geoinf.* **2021**, *103*, 102476. [[CrossRef](#)]
11. Xu, H.; Chen, F.; Zhou, W. A comparative case study of MTInSAR approaches for deformation monitoring of the cultural landscape of the Shanhaiguan section of the Great Wall. *Herit. Sci.* **2021**, *9*, 71. [[CrossRef](#)]
12. Bosiljkov, V.; Uranjek, M.; Arni, R.; Bokan-Bosiljkov, V. An integrated diagnostic approach for the assessment of historic masonry structures. *J. Cult. Herit.* **2010**, *11*, 239–249. [[CrossRef](#)]
13. Pasek, J.; Gaya, H.P. Numerical simulations of the influence of temperature changes on structural integrity of stone temples in Angkor, Cambodia. *Appl. Math. Comput.* **2015**, *267*, 409–418. [[CrossRef](#)]
14. Gigli, G.; Frodella, W.; Mugnai, F.; Tapete, D.; Cigna, F.; Fanti, R.; Intrieri, E.; Lombardi, L. Instability mechanisms affecting cultural heritage sites in the Maltese Archipelago. *Nat. Hazards Earth Syst. Sci.* **2012**, *12*, 1883–1903. [[CrossRef](#)]
15. Chen, F.; Xu, H.; Zhou, W.; Deng, W.; Parcharidis, I. Three-dimensional deformation monitoring and simulations for the preventive conservation of architectural heritage: A case study of the Angkor Wat Temple, Cambodia. *Glsci. Remote Sens.* **2021**, *58*, 217–234. [[CrossRef](#)]
16. Nuttens, T.; Wulf, A.D.; Deruyter, G.; Stal, C. Deformation monitoring with terrestrial laser scanning: Measurement and processing optimization through experience. *Int. Multidiscip. Sci. GeoConf.-SGEM* **2012**, 707–714. [[CrossRef](#)]
17. Tapete, D.; Cigna, F. Site-specific analysis of deformation patterns on archaeological heritage by satellite radar interferometry. *MRS Online Proc. Libr. (OPL)* **2012**, *1374*, 283–295. [[CrossRef](#)]
18. Suziedelyte-Visockiene, J.; Bagdziunaite, R.; Malys, N.; Maliene, V. Close-range photogrammetry enables documentation of environment-induced deformation of architectural heritage. *Environ. Eng. Manag. J.* **2015**, *14*, 1371–1381. [[CrossRef](#)]
19. Garziera, R.; Amabili, M.; Collini, L. Structural health monitoring techniques for historical buildings. In Proceedings of the IV Pan American Conference for Non Destructive Testing, Buenos Aires, Argentina, 22–26 October 2007; pp. 1–12.
20. Sigurdardottir, D.H.; Glisic, B. On-site validation of fiber-optic methods for structural health monitoring: Streicker Bridge. *J. Civil Struct. Health Monit.* **2015**, *5*, 529–549. [[CrossRef](#)]
21. Tapete, D.; Fanti, R.; Cecchi, R.; Petrangeli, P.; Casagli, N. Satellite radar interferometry for monitoring and early-stage warning of structural instability in archaeological sites. *J. Geophys. Eng.* **2012**, *9*, 10–25. [[CrossRef](#)]
22. Parcharidis, I.; Fomelis, M.; Pavlopoulos, K.; Kourkouli, P. Ground deformation monitoring in cultural heritage areas by time series interferometry: The case of ancient Olympia site (western Greece). *Int. Geosci. Remote Sens. Symp.* **2010**.
23. Cigna, F.; Lasaponara, R.; Masini, N.; Milillo, P.; Tapete, D. Persistent scatterer interferometry processing of COSMO-SkyMed StripMap HIMAGE time series to depict deformation of the historic centre of Rome, Italy. *Remote Sens.* **2014**, *6*, 12593–12618. [[CrossRef](#)]
24. Themistocleous, K.; Cuca, B.; Agapiou, A.; Lysandrou, V.; Tzouvaras, M.; Hadjimitsis, D.; Kyriakides, P.; Kouhartsiouk, D.; Margottini, C.; Spizzichino, D.; et al. The protection of cultural heritage sites from Geo-Hazards: The PROTHEGO project. In Proceedings of the 6th International Conference, EuroMed 2016, Nicosia, Cyprus, October 31–November 5 2016; pp. 91–98.
25. Chen, F.; Zhou, W.; Xu, H.; Parcharidis, I.; Lin, H.; Fang, C. Space technology facilitates the preventive monitoring and preservation of the Great Wall of the Ming dynasty: A comparative study of the Qingtongxia and Zhangjiakou sections in China. *IEEE J. Sel. Top. Appl. Earth Obs. Remote Sens.* **2020**, *13*, 5719–5729. [[CrossRef](#)]
26. Gaber, A.; Darwish, N.; Koch, M. Minimizing the residual topography effect on interferograms to improve DInSAR results: Estimating land subsidence in Port-Said city, Egypt. *Remote Sens.* **2017**, *9*, 752. [[CrossRef](#)]
27. Zebker, H.A.; Rosen, P.; Goldstein, R.M.; Gabriel, A.; Werner, C.L. On the derivation of coseismic displacement fields using differential radar interferometry: The Landers earthquake. *J. Geophys. Res.* **1994**, *99*, 19617–19634. [[CrossRef](#)]
28. Du, Y.; Zhang, L.; Feng, G.; Lu, Z.; Sun, Q. On the accuracy of topographic residuals retrieved by MTInSAR. *IEEE Trans. Geosci. Remote Sens.* **2017**, *55*, 1053–1065. [[CrossRef](#)]
29. Ducret, G.; Doin, M.P.; Grandin, R.; Lasserre, C.; Guillaso, S. Dem corrections before unwrapping in a Small Baseline strategy for InSAR time series analysis. *IEEE Geosci Remote Sens. Lett.* **2013**, *11*, 696–700. [[CrossRef](#)]
30. Bayer, B.; Schmidt, D.; Simoni, A. The influence of external digital elevation models on PS-InSAR and SBAS results: Implications for the analysis of deformation signals caused by slow moving landslides in the Northern Apennines (Italy). *IEEE Trans. Geosci. Remote Sens.* **2017**, *55*, 2618–2631. [[CrossRef](#)]
31. Ferretti, A.; Prati, C.; Rocca, F. Permanent scatterers in SAR interferometry. *IEEE Trans. Geosci. Remote Sens.* **2001**, *39*, 8–20. [[CrossRef](#)]
32. Berardino, P.; Fornaro, G.; Lanari, R. A new algorithm for surface deformation monitoring based on small baseline differential SAR interferograms. *IEEE Trans. Geosci. Remote Sens.* **2002**, *40*, 2375–2383. [[CrossRef](#)]

33. Samsonov, S. Topographic correction for ALOS PALSAR interferometry. *IEEE Trans. Geosci. Remote Sens.* **2010**, *48*, 3020–3027. [[CrossRef](#)]
34. Fattahi, H.; Amelung, F. Dem error correction in InSAR time series. *IEEE Trans. Geosci. Remote Sens.* **2013**, *51*, 4249–4259. [[CrossRef](#)]
35. Zhang, L.; Jia, H.; Lu, Z.; Liang, H.; Ding, X.; Li, X. Minimizing height effects in MTInSAR for deformation detection over built areas. *IEEE Trans. Geosci. Remote Sens.* **2019**, *57*, 9167–9176. [[CrossRef](#)]
36. Rosen, P.A.; Hensley, S.; Joughin, I.R.; Li, F.K.; Madsen, S.N.; Rodriguez, E.; Goldstein, R.M. Synthetic aperture radar interferometry. *Proc. IEEE* **2000**, *88*, 333–380. [[CrossRef](#)]
37. Massonnet, D.; Rossi, M.; Carmona, C.; Adragna, F.; Peltzer, G.; Feigl, K.; Rabaute, T. The displacement field of the Landers earthquake mapped by radar interferometry. *Nature* **1993**, *364*, 138–142. [[CrossRef](#)]
38. Zhang, Q.; Yu, Q.; Cheng, J.; Wang, C. Characteristics of 3" SRTM Errors in China. *Geomat. Inf. Sci. Wuhan Univ.* **2018**, *43*, 684–690. [[CrossRef](#)]
39. Werner, M. Shuttle radar topography mission (SRTM) mission overview. *Frequenz* **2001**, *55*, 75–79. [[CrossRef](#)]
40. Tachikawa, T.; Hato, M.; Kaku, M.; Iwasaki, A. Characteristics of ASTER GDEM version 2. *Int. Geosci. Remote Sens. Symp.* **2011**, 3657–3660. [[CrossRef](#)]
41. Gao, M.; Gong, H.; Li, X.; Chen, B.; Zhou, C.; Shi, M.; Guo, L.; Chen, Z.; Ni, Z.; Duan, G. Imaging land subsidence induced by groundwater extraction in Beijing (China) using satellite radar interferometry. *Remote Sens.* **2019**, *11*, 1466. [[CrossRef](#)]
42. Gao, M.; Gong, H.; Li, X.; Chen, B.; Duan, G. Land subsidence and ground fissures in Beijing Capital International Airport (BCIA): Evidence from Quasi-PS InSAR analysis. *Remote Sens.* **2019**, *11*, 1466. [[CrossRef](#)]
43. Chen, B.; Gong, H.; Chen, Y.; Li, X.; Zhao, X. Land subsidence and its relation with groundwater aquifers in Beijing Plain of China. *Sci. Total Environ.* **2020**, *735*, 139111. [[CrossRef](#)] [[PubMed](#)]
44. Zhou, C.; Lan, H.; Gong, H.; Zhang, Y.; Warner, T.A.; Clague, J.J.; Wu, Y. Reduced rate of land subsidence since 2016 in Beijing, China: Evidence from Tomo-PSInSAR using RadarSAT-2 and Sentinel-1 datasets. *Int. Remote Sens.* **2019**, *41*, 1259–1285. [[CrossRef](#)]
45. Su, M.; Wall, G. Global-local relationships and governance issues at the Great Wall world heritage site. *China J Sustain. Tour.* **2012**, *20*, 1067–1086. [[CrossRef](#)]
46. Liu, Y.; Gao, J.; Yang, Y. A Holistic approach towards assessment of severity of land degradation along the Great Wall in northern Shaanxi province. *China Environ. Monit Assess.* **2003**, *82*, 187–202. [[CrossRef](#)] [[PubMed](#)]
47. Deng, F.; Zhu, X.; Li, X.; Li, M. 3D digitisation of large-scale unstructured Great Wall heritage sites by a small unmanned helicopter. *Remote Sens.* **2017**, *9*, 423. [[CrossRef](#)]
48. Hua, W.; Qiao, Y.; Hou, M. The Great Wall 3D documentation and application based on multisource data fusion—A case study of No.15 enemy tower of the new Guangwu Great Wall. *Int. Arch. Photogramm. Remote Sens. Spat. Inf. Sci.* **2020**, *43*, 176–181. [[CrossRef](#)]
49. Wang, J.; Fu, C. Analysis on the city wall stability for Shanhaiguan section of the Great Wall. *J. Eng. Geol.* **2006**, *14*, 301–307.
50. Gabriel, A.K.; Goldstein, R.M.; Zebker, H.A. Mapping small elevation changes over large areas: Differential radar interferometry. *J. Geophys. Res. Solid Earth.* **1989**, *94*, 9183–9191. [[CrossRef](#)]
51. Tang, P.; Chen, F.; Guo, H.; Tian, B.; Wang, X.; Natarajan, I. Large-area landslides monitoring using advanced multi-temporal InSAR technique over the giant panda habitat, Sichuan, China. *Remote Sens.* **2015**, *7*, 8925–8949. [[CrossRef](#)]
52. Jia, Y.; Chen, X.; Li, J. Error analysis of multi-source ground elevation data of mountain area. *Arid Land Geogr.* **2014**, *37*, 793–801. [[CrossRef](#)]
53. Chen, F.; Liu, H.; Xu, H.; Zhou, W.; Balz, T.; Chen, P.; Zhu, X.; Lin, H.; Fang, C.; Parcharidis, I. Deformation monitoring and thematic mapping of the Badaling Great Wall using very high-resolution interferometric synthetic aperture radar data. *Int. J. Appl. Earth Obs.* **2021**, *105*, 102630. [[CrossRef](#)]
54. Montazeri, S.; Xiao, X.Z.; Eineder, M.; Bamler, R. Three-dimensional deformation monitoring of urban infrastructure by tomographic SAR using multitrack TerraSAR-X data stacks. *IEEE Trans. Geosci. Remote Sens.* **2016**, *54*, 6868–6878. [[CrossRef](#)]
55. Milillo, P.; Fielding, E.J.; Shulz, W.H.; Delbridge, B.; Burgmann, R. Cosmo-SkyMed spotlight interferometry over rural areas: The slumgullion landslide in Colorado, USA. *IEEE J. Sel. Top Appl. Earth Obs. Remote Sens.* **2014**, *7*, 2919–2926. [[CrossRef](#)]
56. Schneider, R.Z.; Papathanassiou, K.P.; Hajnsek, I.; Moreira, A. Polarimetric and interferometric characterization of coherent scatterers in urban areas. *IEEE Trans. Geosci. Remote Sens.* **2006**, *44*, 971–984. [[CrossRef](#)]
57. Dong, J.; Zhang, L.; Tang, M.; Liao, M.; Xu, Q.; Gong, J.; Ao, M. Mapping landslide surface displacements with time series SAR interferometry by combining persistent and distributed scatterers: A case study of Jiayu landslide in Danba, China. *Remote Sens. Environ.* **2018**, *205*, 180–198. [[CrossRef](#)]
58. Yu, C.; Li, Z.; Penna, N.T.; Crippa, P. Generic atmospheric correction model for Interferometric Synthetic Aperture Radar observations. *J. Geophys. Res. Solid Earth* **2018**, *123*, 9202–9222. [[CrossRef](#)]
59. Bekaert, D.P.S.; Hooper, A.; Wright, T.J. A spatially variable power law tropospheric correction technique for InSAR data. *J. Geophys. Res. Solid Earth* **2015**, *120*, 1345–1356. [[CrossRef](#)]